

High-Resolution Sensing via Quantum States Discrimination

Qi-An Su,* Qi Song,* Hongjing Li,[†] Kaiwen Fu, Xingyu Wu, Jingzheng Huang, Chuan Wang, and Guihua Zeng

State Key Laboratory of Photonics and Communications,

*Institute for Quantum Sensing and Information Processing, School of Automation and Intelligent Sensing,
Shanghai Jiao Tong University, Shanghai, 200240, People's Republic of China*

(Dated: December 22, 2025)

High-resolution sensing plays a significant role in scientific research and industrial production, but the practical implementation is constrained by the physical mechanisms of the sensors. To address the critical limitation, we propose a high-resolution sensing approach based on quantum state discrimination. Distinct from conventional strategies, the proposed approach constructs measurement operators in the orthogonal complement space rather than eigenspace of the eigenstate, thereby notably improving the discriminability among quantum states. Moreover, the experimental results via an optical microcavity demonstrate a potential sensing resolution of 4×10^{-6} °C and 18 $\mu\epsilon$ respectively for temperature and strain, and further verify the feasibility of simultaneous sensing of the two parameters. This work establishes a universal approach for high-resolution sensing, and may be extended to different sensing platforms across various application scenarios.

Introduction— Sensing resolution fundamentally defines the lower limit of detectable signals for a sensor[1–5]. Crucially, resolution limitation often stems from the coupling of multiple physical phenomena, where interference from extraneous effects can mask the response of the target parameter[6, 7], and the conflation of these effects undermines reliability in multi-parameter sensing[8, 9]. In microcavity sensing via transmission spectrum analysis, spectral resolution is limited by spontaneous emission-induced resonance broadening and shifts caused by refractive index and optical path changes[10–13]. For distributed optical fiber sensing, measurement and spatial resolution are constrained by cross-sensitivity among Brillouin, Raman, and Rayleigh scattering mechanisms, as well as by the specific demodulation techniques employed[14, 15]. Clearly, these inherent physical constraints significantly complicate the extraction and processing of complex sensor data. Although machine learning offers promise for enhancing data interpretation[16–18], the practical implementation is hindered by the high cost of acquiring training data[17, 19, 20] and by the inherent inability to surpass the fundamental physical limits of the sensing mechanisms themselves.

Quantum state discrimination offers an alternatively promising approach for parameter sensing due to a profound mathematical isomorphism between the two frameworks. Constrained by the Heisenberg uncertainty principle[21–24], quantum state discrimination theory aims to identify optimal measurement operators that maximize the distinguishability of non-orthogonal quantum states[24–27]. In the minimum error discrimination framework, the average error probability is minimized through optimization of the measurement strategy, making it suitable when prior probabilities of the states are known and a finite error rate is acceptable[28–30]. In contrast, unambiguous state discrimination ensures strictly correct identification at the expense of allowing inconclusive outcomes, thereby trading success probability for

certainty[31–33, 43]. However, in practical sensing applications, the distinguishability among encoded quantum states is often exceedingly low, necessitating improvements in quantum hardware preparation, increased measurement complexity, and a larger number of probe states challenges that pose significant limitations to current quantum state discrimination methodologies.

In this paper, we present a high-resolution sensing approach based on quantum state discrimination. By encoding unknown parameters on quantum states and employing quantum state discrimination techniques, we can effectively identify and extract the target parameters. In contrast to conventional quantum state discrimination approaches, our method utilizes the orthogonal complement space of the quantum states rather than the eigenspace itself, thereby significantly enhancing the distinguishability among quantum states. Furthermore, we experimentally validate the feasibility of this approach on a whispering gallery mode (WGM) microcavity platform. The results demonstrate resolutions of 4×10^{-6} °C for temperature and 18 $\mu\epsilon$ for strain in single-parameter sensing, and confirm the capability for simultaneous temperature and strain sensing. The proposed approach not only introduces a new methodology for parameter sensing but also offers insights applicable to quantum state discrimination in broader contexts.

Model Setup— The schematic of high-resolution sensing based on quantum state discrimination is illustrated in Fig.1a. The approach comprises four stages: quantum state evolution, measurement via pre-defined measurement operators, sensitivity factor generation, and parameter retrieval via quantum state determination. In the quantum state evolution stage, the unknown parameter vector \mathbf{x} , which involves several unknown parameters, is encoded into the initial quantum state ρ_0 , yielding an evolution of

$$\rho_0 \rightarrow \rho_x. \quad (1)$$

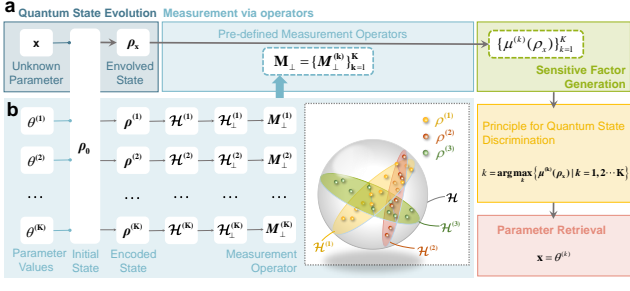


FIG. 1. The basic concept of quantum state discrimination. **a** Quantum state discrimination process. It consists of four stages: quantum state evolution, measurement via pre-defined measurement operators, sensitivity factor generation and parameter retrieval via quantum state discrimination. **b** Schematic illustration of the eigenspace and orthogonal complement space. The entire sphere represents the total eigenspace \mathcal{H} encompassing all quantum states. Taking three eigenspaces as an example, the planes within the sphere represent individual eigenspace $\mathcal{H}^{(k)}$, while the dots within the planes mark the possible positions of quantum state $\rho^{(k)}$. The regions of the sphere excluding the planes correspond to orthogonal complement space $\mathcal{H}_{\perp}^{(k)}$.

After that, the evolved state ρ_x is measured by the pre-defined measurement operator $\mathbf{M}_{\perp} = \{M_{\perp}^{(k)}, k = 1, 2, \dots, K\}$. As depicted in Fig.1b, each element $M_{\perp}^{(k)}$ in \mathbf{M}_{\perp} quantifies the probability that a given quantum state lies within the orthogonal complement subspace $\mathcal{H}_{\perp}^{(k)}$, which is constructed from K sets of known distinct parameters $\boldsymbol{\theta} = \{\boldsymbol{\theta}^{(k)}, k = 1, 2, \dots, K\}$. It is worth noting that the probability of the encoded state $\rho^{(k)}$ in $\mathcal{H}_{\perp}^{(k)}$ is definitely zero, whereas other quantum states exhibit a non-zero possibility of occupying the subspace. Quantum states with high inherent distinguishability can be directly distinguished by eigenspace $\mathcal{H}^{(k)}$ which is constructed from the eigenstates of the quantum state and is hereafter referred to simply as the eigenspace. Indeed, in practical scenarios, small differences in parameters lead to similar quantum states, thereby causing overlap in the eigenspace. Therefore, the orthogonal complement space is selected as decision space.

Based on the measurement results, the sensitivity factor $\boldsymbol{\mu}_{\perp}(\rho_x) = \{\mu_{\perp}^{(k)}(\rho_x), k = 1, 2, \dots, K\}$ is defined to quantitatively characterize the dissimilarity between the unknown ρ_x and the pre-calibrated states $\{\rho^{(k)}, k = 1, 2, \dots, K\}$, i.e.,

$$\mu_{\perp}^{(k)}(\rho_x) = \frac{1}{D_{\perp}^{(k)}(\rho_x)}. \quad (2)$$

Here the probability distance $D_{\perp}^{(k)}(\rho_x)$ is used to characterize the difference in the occupancy probabilities in

$\mathcal{H}_{\perp}^{(k)}$ between ρ_x and the encoded state $\rho^{(k)}$, i.e.,

$$D_{\perp}^{(k)}(\rho_x) = |\text{tr}(M_{\perp}^{(k)\dagger} \rho^{(k)} M_{\perp}^{(k)}) - \text{tr}(M_{\perp}^{(k)\dagger} \rho_x M_{\perp}^{(k)})| = \text{tr}(M_{\perp}^{(k)\dagger} \rho_x M_{\perp}^{(k)}). \quad (3)$$

Subsequently, the unknown state ρ_x is identified as $\rho^{(\tilde{k})}$, where

$$\tilde{k} = \arg \max_k \{\mu_{\perp}^{(k)}(\rho_x), k = 1, 2, \dots, K\}, \quad (4)$$

and the unknown parameter vector \mathbf{x} can be judged as $\boldsymbol{\theta}^{(\tilde{k})}$, the \tilde{k} -th set of parameters. Parameters within a specific range can be mapped to these distinct eigenspaces, enabling discrete representations for the parameter space. The framework establishes a theoretical basis for analyzing parameter resolution using quantum state discrimination.

To further evaluate the sensing resolution of the proposed method, we consider the dimension of total eigenspace \mathcal{H} is D . In this case, arbitrary linearly independent eigenstates of \mathcal{H} can form a subspace of \mathcal{H} . The maximal number of mutually distinct subspaces is given by

$$N_{\max} = \begin{cases} \frac{D!}{(\frac{D}{2})!^2}, & D \text{ is even;} \\ \frac{D!}{\frac{D-1}{2}! \frac{D+1}{2}!}, & D \text{ is odd.} \end{cases} \quad (5)$$

Experimental verification— To validate the feasibility, WGM microcavity serves as the sensing unit, and the conceptual design of our approach is shown in Fig.2a. The initial state ρ_0 should carry the parameter information induced by microcavity sensing and thereby the probe light is required to span a wide spectral range, so it can be either an optical frequency comb or a broadband light source. After sensing with the WGM microcavity, the parameter vector \mathbf{x} is encoded onto ρ_0 , leading to the evolution of $\rho_0 \rightarrow \rho_x$. As depicted in Fig.2b, we conduct experiments taking temperature and stress sensing as examples. Temperature and strain are respectively acting on the WGM microcavity and the tapered fiber, inducing dispersive and dissipative responses that result in a resonant frequency shift and a change in resonance broadening[35–38]. These effects are also evident in the collective pattern of WGM microcavity transmission, which has been demonstrated to have superior sensitivity, precision, noise robustness, and parameter discrimination capabilities compared to single-mode cavity sensing approaches[39]. After that, the evolved state ρ_x is ultimately judged as a specific known quantum state $\rho^{(\tilde{k})}$ based on the sensitivity factor $\boldsymbol{\mu}_{\perp}(\rho_x)$ acquired through the measurement operator \mathbf{M}_{\perp} . Finally, the unknown parameter vector \mathbf{x} can be retrieved as $\boldsymbol{\theta}^{(\tilde{k})}$ by combining the correspondence between parameters and quantum states. Constrained by the quality factor of the WGM

microcavity and the performance of the detection spectrometer, the total eigenspace \mathcal{H} with a dimension of 25 allows up to 10^6 distinguishable quantum states as defined by Eq. (5), which determines the fundamental resolution limit.

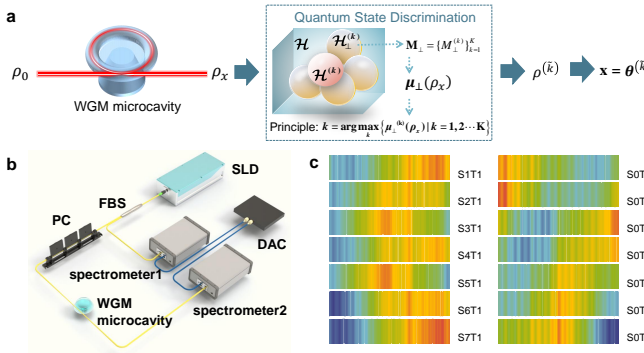


FIG. 2. Conceptual design and experimental setup. **a** Conceptual design. **b** Experimental setup. The abbreviations are as follows: SLD: superluminescent diode; FBS: fiber beam splitter; PC: polarization controller; WGM: whispering gallery mode microcavity; DAC: data acquisition card. **c** Visualization of transmission spectra under two sets of conditions: varying strains at a fixed temperature, and a fixed strain at varying temperatures. Distinct positions corresponding to different frequencies and colors indicating the magnitude at each frequency. The meanings of the letters are as follows: T: temperature, S: strain.

In the following, we conducted two sets of experiments: one involves separate sensing of temperature and strain, while the other is designed for the simultaneous sensing of these two parameters. The detected transmissions form the data set, where there are several samples associated with the specific parameter values. From Fig. 2c, it is clear that the contribution of the alternative mechanism remains evident even when a single sensing mechanism is employed. Furthermore, the identification of both sensing mechanisms would not only enable parameter sensing with effective noise suppression but also allow the development of multi-parameter sensing strategies to extract additional information[6, 7, 40, 41]. For experimental evaluation, the sensitivity factors $\mu_{\perp}(\rho_x)$ is utilized. As previously discussed, the measurement operators \mathbf{M} can be employed for quantum state discrimination, but they would cause information overlap, which is not conducive to distinction. Given that the effect is more significant in multi-parameter sensing scenarios, a comprehensive analysis is introduced in this part.

The sensing results for dispersion and dissipation responses, characterized by temperature and stress sensing respectively, are presented in Fig. 3a and Fig. 3b. The distribution of sensitivity factor $\mu_{\perp}(\rho_x)$ in Fig. 3a is determined with resolutions of 0.1°C and 0.01°C , and that in Fig. 3b is evaluated at resolutions of $10 \mu\epsilon$ and $1 \mu\epsilon$. The results demonstrate that the proposed approach

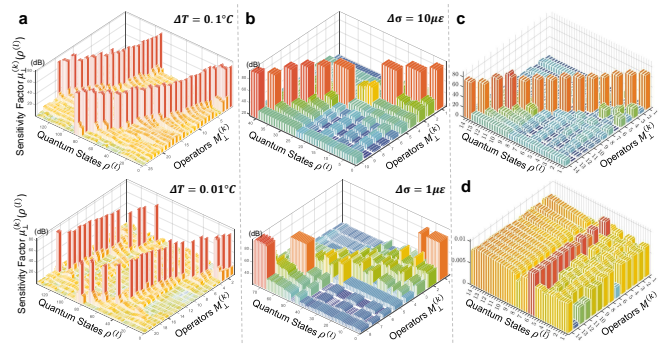


FIG. 3. The distribution of sensitivity factors under different conditions. **a** The distribution of sensitivity factor for temperature sensing under two kinds of resolutions. **b** The distribution of sensitivity factor for strain sensing under two kinds of resolutions. **c** The distribution of sensitivity factor under \mathbf{M}_{\perp} . **d** The distribution of sensitivity factor under \mathbf{M} .

enables clear discrimination even in the presence of interfering effects. Moreover, the disparity in sensitivity factors between correctly and incorrectly classified samples decreases markedly when the parameter resolution is increased by an order of magnitude. According to prior analysis, the maximum achievable resolutions for temperature and strain are $4 \times 10^{-6}^{\circ}\text{C}$ and $18 \mu\epsilon$, respectively.

For multi-parameter sensing, we investigate the superiority of using the orthogonal complement space as the decision space. The distributions of sensitivity factors under the operators \mathbf{M}_{\perp} and \mathbf{M} are respectively shown in Fig. 3c and Fig. 3d. As illustrated in Fig. 3c, the obtained factors with \mathbf{M}_{\perp} exhibit a difference exceeding 30 dB between correct and incorrect identifications, whereas those obtained with \mathbf{M} in Fig. 3d are mostly around 0.01 dB, demonstrating the advantage of the proposed approach. Additionally, since the maximum number of distinguishable quantum states in this experiment is fixed, though the resolution limits of both parameters are subject to a trade-off governed by the specific requirements of different experimental conditions, the resolution can progressively approach $4 \times 10^{-6}^{\circ}\text{C}$ for temperature and $18 \mu\epsilon$ for strain, corresponding to the resolution achievable in single-parameter sensing.

Discussion— In summary, to address the inherent physical constraints on sensing resolution, we propose a high-resolution sensing approach by encoding the unknown parameters onto quantum states and then performing quantum state discrimination to extract the target parameter. The approach exploits the significantly enhanced distinguishability offered by utilizing the orthogonal complement eigenspace of the quantum states, diverging from previous methods that utilized the eigenspace, and the resolution limit is governed by the dimension of the total eigenspace \mathcal{H} .

To further validate the feasibility, a whispering gallery mode (WGM) microcavity is employed as the sensing

unit with broadband light as the probe light and a cost-effective spectrometer for detection. In the configuration, the dimension of the total eigenspace is governed by the microcavity quality factor and the spectrometers detection range. Even with an optimized quality factor of 10^5 and a low-cost spectrometer, the eigenspace spans 25 dimensions, enabling the discrimination of up to $\sim 10^6$ distinct quantum states, thereby achieving temperature and strain resolutions of 4×10^{-6} °C and 18 pε. Despite relying on relatively modest experimental instrumentation, the proposed method achieves superior resolution. Further enhancements are expected through optimization of the microcavity design to achieve higher quality factors. When the WGM microcavity mode is stably maintained at a quality factor of 10^5 , the dimensionality increases to 40, corresponding to a maximum of approximately 10^{11} distinguishable quantum states.

The method exhibits broad platform compatibility, extending beyond broadband light sources and WGM microcavities. It can be implemented with any light source exhibiting sufficient spectral coverage over the target range and integrated with sensing platforms featuring broad transmission spectra, such as fiber microcavities[42–44] and photonic crystal [45, 46]. Owing to the cost-effectiveness and ease of integration, the proposed approach holds significant potential for advancing practical applications, including wearable physiological monitoring in healthcare[47–50], intelligent electronic skins via highly sensitive environmental sensing[51–53], and rapid characterization of electrical properties in materials science[54–57].

Acknowledgments— This work was supported by the National Natural Science Foundation of China (No. 62471289, and No. 62131002), Natural Science Foundation of Shanghai (No. 24ZR1432900), Quantum Science and Technology-National Science and Technology Major Project (No.2021ZD0300703) and Shanghai Municipal Science and Technology Major Project (No. 2019SHZDZX01).

and ultra-large-dynamic-range fiber temperature sensor based on continuous resonance peaks tracking technique, *Opt. Laser Technol.* **181**, 112000 (2025).

- [5] H. Y. Xu, S. C. Chen, S. F. Ren, *et al.*, High-Resolution Spectrum Reconstruction of Cascaded FBG-FPI Sensor in Resource-Constrained Environments, *IEEE Sensors J.* **24**, 11878-11885 (2024).
- [6] J. J. Tian, Y. Z. Jiao, Q. Fu, S. B. Ji, Z. G. Li, M. R. Quan, and Y. Yao, A Fabry-Perot interferometer strain sensor based on concave-core photonic crystal fiber, *J. Lightw. Technol.* **36**, 1952-1958 (2018).
- [7] A. Wada, S. Tanaka, and N. Takahashi, Fast and high-resolution simultaneous measurement of temperature and strain using a Fabry-Perot interferometer in polarization-maintaining fiber with laser diodes, *J. Lightw. Technol.* **36**, 1011-1017 (2018).
- [8] C. H. Wei, Q. Liu, D. D. Lin, D. Zhu, J. Z. Shi, and Y. P. Wang, High-Precision Cross-Sensitivity Mitigation Using CNN-BiLSTM for Multiparameter Optical Sensing, *IEEE Sensors J.* **25**, 21600-21607 (2025).
- [9] G. L. Chen, J. Li, H. M. Zhu, Y. Y. Wang, H. Y. Ji, and F. L. Meng, Optical fiber gas sensor with multiparameter sensing and environmental anti-interference performance, *J. Ind. Inf. Integr.* **38**, 100565 (2024).
- [10] X. L. Hao, S. Y. Zhao, J. J. Gao, and L. J. Suo, All-optical tunable whispering gallery mode lasing in a PMMA-coated microcavity embedded with a high-efficiency nanoheater, *Opt. Laser Technol.* **164**, 109527 (2023).
- [11] X. W. Li, R. B. Bai, L. Y. Du, W. L. Zhang, and M. Li, Femtosecond Laser Fabrication and Refractive Index Sensing Characteristics of Highly Sensitive Fiber Michelson Microcavity, *IEEE Sensors J.* **24**, 1432-1442 (2024).
- [12] Y. X. Zhang, Y. J. Cai, Y. X. Zhou, Y. H. Liu, H. Hu, and T. Lin, Effects of Epoxy Molecular Structure on Photoelastic Properties for Micro-Stress Optical Measurement, *J. Appl. Polym. Sci.* **142**, 70062 (2025).
- [13] V. N. Naunyka, V. V. Shepelevich, A. V. Makarevich, and S. M. Shandarov, Influence of Photoelastic and Piezoelectric Effects on the Energetic Characteristics of Transmission and Reflection Holograms in a Photorefractive Crystal, *J. Appl. Spectrosc.* **87**, 712-719 (2020).
- [14] K. Naeem, C. Lee, K. Linganna, C. Kang, M. K. Oh, N. E. Yu, H. Kang, and B. H. Kim, Multiparameter Distributed Fiber Sensor Based on Optical Frequency-Domain Reflectometry and Bandwidth-Division Multiplexing, *IEEE Sensors J.* **21**, 25703-25709 (2021).
- [15] E. Ip, J. Fang, Y. W. Li, Q. Wang, M.-F. Huang, M. Salemi, and Y.-K. Huang, Distributed fiber sensor network using telecom cables as sensing media: technology advancements and applications, *J. Opt. Commun. Netw.* **14**, A61-A68 (2022).
- [16] E. A. Tcherniavskaya and V. A. Saetchnikov, Application of neural networks for classification of biological compounds from the characteristics of whispering-gallery-mode optical resonance, *J. Appl. Spectrosc.* **78**, 457-460 (2011).
- [17] D. Hu, C. L. Zou, H. L. Ren, *et al.*, Multi-Parameter Sensing in a Multimode Self-Interference Micro-Ring Resonator by Machine Learning, *Sensors* **20**, 709 (2020).
- [18] K. P. Nascimento, A. Frizera-Neto, C. Marques, and A. G. Leal-Junior, Machine learning techniques for liquid level estimation using FBG temperature sensor array, *Opt. Fiber Technol.* **65**, 102612 (2021).

* These authors contributed equally to this work.

† lhjnet2012@sjtu.edu.cn

- [1] H. W. Chen, Z. D. Wang, B. Shen, and J. L. Liang, Distributed Recursive Filtering Over Sensor Networks With Nonlogarithmic Sensor Resolution, *IEEE Trans. Autom. Control* **67**, 5408-5415 (2022).
- [2] H. Y. Wang, S. Y. Fan, L. Z. Meng, *et al.*, Multiparameter sensor based on cascaded multicore FBGs and an FPI for bending, temperature and pressure measurements, *Opt. Laser Technol.* **175**, 110782 (2024).
- [3] H. C. Li, M. G. Lou, W. Z. Huang, and W. T. Zhang, Fiber Optic Strain Sensor With Femto-Strain Resolution Based on Differentiating Interferometer, *J. Lightwave Technol.* **42**, 6360-6366 (2024).
- [4] W. Jin, Y. F. Lu, J. X. Gao, *et al.*, Ultra-high-resolution

[19] S. Ren, S. C. Chen, J. L. Yang, *et al.*, High-efficiency FBG array sensor interrogation system via a neural network working with sparse data, *Opt. Express* **31**, 8937-8952 (2023).

[20] K. Dey, V. Nikhil, and S. Roy, Machine learning approach with higher accuracy for simultaneous measurement of the dual parameter by MSM fiber structure, *Measurement* **221**, 113426 (2023).

[21] J. Polo-Gómez, Thermodynamic bound on quantum state discrimination, *Phys. Rev. E* **109**, 014119 (2024).

[22] N. Gisin, Quantum cloning without signaling, *Phys. Lett. A* **242**, 1-3 (1998).

[23] Y. L. Hu and M. Tomamichel, Fundamental limits on quantum cloning from the no-signaling principle, *Phys. Rev. A* **109**, 022221 (2024).

[24] G. Jaeger and A. Shimony, Optimal distinction between two non-orthogonal quantum states, *Phys. Lett. A* **197**, 83-87 (1995).

[25] J. A. Bergou, Quantum state discrimination and selected applications, *J. Phys.: Conf. Ser.* **84**, 012001 (2007).

[26] S. M. Barnett and S. Croke, Quantum state discrimination, *Adv. Opt. Photon.* **1**, 238-278 (2009).

[27] J. Bae and L. C. Kwek, Quantum state discrimination and its applications, *J. Phys. A: Math. Theor.* **48**, 083001 (2015).

[28] C. W. Helstrom, Quantum detection and estimation theory, *J. Stat. Phys.* **1**, 231-252 (1969).

[29] J. Bae, Structure of minimum-error quantum state discrimination, *New J. Phys.* **15**, 073037 (2013).

[30] G. M. Nikolopoulos, Minimum-error state discrimination and Fano's inequality, *Am. J. Phys.* **93**, 566-573 (2025).

[31] I. D. Ivanovic, How to differentiate between non-orthogonal states, *Phys. Lett. A* **123**, 257-259 (1987).

[32] D. Dieks, Overlap and distinguishability of quantum states, *Phys. Lett. A* **126**, 303-306 (1988).

[33] S. Croke, E. Andersson, S. M. Barnett, C. R. Gilson, and J. Jeffers, Maximum Confidence Quantum Measurements, *Phys. Rev. Lett.* **96**, 070401 (2006).

[34] S. J. Zhang and W. H. Zhang, Unambiguous correct discrimination of real quantum states, *J. Mod. Opt.* **70**, 533-540 (2023).

[35] K. M. Kareh, Whispering-gallery-mode sensors for biological and physical sensing, *Nat. Rev. Methods Primers* **1**, 82 (2021).

[36] J. W. Meng, S. J. Tang, J. Sun, K. Shen, C. Li, Q. Gong, and Y. F. Xiao, Dissipative Acousto-optic Interactions in Optical Microcavities, *Phys. Rev. Lett.* **129**, 073901 (2022).

[37] X. Cao, H. Yang, Z. L. Wu, *et al.*, Ultrasound sensing with optical microcavities, *Light Sci Appl* **13**, 159 (2024).

[38] Q. Song, H. J. Li, C. X. Yu, *et al.*, High-sensitivity Optical Microcavity Acoustic Sensor Covering Free Spectral Range, *arXiv:2508.10229* (2025).

[39] J. Liao and L. Yang, Optical whispering-gallery mode barcodes for high-precision and wide-range temperature measurements, *Light Sci Appl* **10**, 32 (2021).

[40] B. Pang, Z. T. Gu, Q. Ling, W. Y. Wu, and Y. Zhou, Simultaneous measurement of temperature and surrounding refractive index by superimposed coated long period fiber grating and fiber Bragg grating sensor based on mode barrier region, *Optik* **220**, 165136 (2020).

[41] S. H. Zhang, Y. Guo, T. L. Cheng, S. G. Li, and J. S. Li, Surface plasmon resonance sensor based on a D-shaped photonic crystal fiber for high and low refractive index detection, *Optik* **212**, 164697 (2020).

[42] L. N. Wang, Y. F. Geng, X. J. Li, D. Yi, Z. F. Tong, T. T. Duan, S. L. Chen, and X. M. Hong, High-Resolution Optical Fiber Salinity Sensor With Self-Referenced Parallel Fabry-Perot Fiber Microcavity, *IEEE Sens. J.* **23**, 337-343 (2023).

[43] H. L. Zhang, J. W. Zhang, X. T. Yang, H. C. Zhang, and J. R. Yang, Intensity-Modulated Fiber-Optic Salinity Sensor by Tapered Microcavity Mach-Zehnder Interferometer, *IEEE Sensors J.* **23**, 22517-22523 (2023).

[44] H. L. Chen, Y. Zheng, B. C. Li, *et al.*, Bubble microcavity strain and gravity sensor with temperature and bending insensitivity using an ultra-thin core optical fiber, *Opt. Laser Technol.* **142**, 107193 (2021).

[45] P. H. Dong, C. Y. Liu, L. Zhang, D. X. Dai, and Y. C. Shi, Reconfigurable add-drop filter based on an antisymmetric multimode photonic crystal nanobeam cavity in a silicon waveguide, *Opt. Express* **30**, 17332-17339 (2022).

[46] C. Wang, Z. Y. Fu, F. J. Sun, J. Zhou, and H. P. Tian, Large-Dynamic-Range Dual-Parameter Sensor Using Broad FSR Multimode Photonic Crystal Nanobeam Cavity, *IEEE Photonics J.* **10**, 1-14 (2018).

[47] C. El-Hajj and P. A. Kyriacou, A review of machine learning techniques in photoplethysmography for the non-invasive cuff-less measurement of blood pressure, *Biomed. Signal Process. Control* **58**, 101870 (2020).

[48] L. Lu, J. Y. Zhang, Y. Xie, F. Gao, S. Xu, X. H. Wu, Z. W. Ye, Wearable Health Devices in Health Care: Narrative Systematic Review, *JMIR Mhealth Uhealth* **8**, e18907 (2020).

[49] D. Ray, T. Collins, S. I. Woolley, and P. V. S. Ponnappalli, A Review of Wearable Multi-Wavelength Photoplethysmography, *IEEE Rev. Biomed. Eng.* **16**, 136-151 (2023).

[50] M. Wang, H. Zheng, L. Yang, and L. Y. Jiang, Multi Parameter Sweat Detection System Based on Screen Printed Electrodes, *Sens. Imaging* **26**, 136 (2025).

[51] G. Tang, Q. F. Shi, Z. X. Zhang, T. Y. Y. He, Z. D. Sun, and C. K. Lee, Hybridized wearable patch as a multi-parameter and multi-functional human-machine interface, *Nano Energy* **81**, 105582 (2021).

[52] C. Shang, Q. H. Xu, N. M. Liang, *et al.*, Multi-parameter e-skin based on biomimetic mechanoreceptors and stress field sensing, *npj Flex Electron* **7**, 19 (2023).

[53] X. T. Dong, Y. L. Yu, Q. C. Yu, K. X. Miao, and Q. Z. Zhou, Multi-parameter tactile sensing and recognition for robotic finger based on Bi-FBG, *Opt. Laser Technol.* **192**, 113634 (2025).

[54] C. G. Juan, B. Potelon, C. Quendo, *et al.*, Study of Qu-based resonant microwave sensors and design of 3D-printed devices dedicated to glucose monitoring, *IEEE Trans. Instrum. Meas.* **70**, 8005716 (2021).

[55] S. P. Hehenberger, S. Caizzone, S. Thurner, and A. G. Yarovoy, Broadband effective permittivity simulation and measurement techniques for 3D-printed dielectric crystals, *IEEE Trans. Microw. Theory Tech.* **71**, 4161-4172 (2023).

[56] J. Persad and S. Rocke, Impact of 3D printing infill patterns on the effective permittivity of 3D printed substrates, *IEEE J. Microw.* **4**, 277-292 (2024).

[57] C. G. Juan, B. Potelon, A. Aquino, *et al.*, Multi-parameter simultaneous extraction with a novel microwave sensor based on coupled resonators, *Sci. Rep.* **14**, 23076 (2024).